Water Practice & Technology

IWA PUBLISHING

Water Practice & Technology Vol 18 No 8, 1742 doi: 10.2166/wpt.2023.119

Rare earth ions (La^{3+}, Nd^{3+}) substituted cobalt–strontium spinel ferrites for photocatalytic degradation of textile dyes

Iram Ahmad[a,f,†], Muhammad Safdar[b], Nazia Yasmin[a,†], Aisha Iftikhar[a], Ambreen Kalsoom[c], Sadia Khalid[d], Zil e Shams[e] and Misbah Mirza[a,*]

[a] Department of Physics, The Women University Multan, Multan, Pakistan
[b] Department of Basic Sciences & Humanities, Khawaja Fareed University of Engineering & Information Technology, Rahim Yar Khan, Pakistan
[c] Department of Physics, The Govt Sadiq College Women University Bahawalpur, Bahawalpur, Pakistan
[d] Nanosciences & Technology Department, National Centre for Physics Shahdra Valley Road Quaid-i-Azam University Campus, Islamabad 45320, Pakistan
[e] The Women University Multan, Multan, Pakistan
[f] Department of Chemical, Material and Production Engineering, DICMaPI University of Naples Federico-II, Naples, Italy
[†] Equal authors.
*Corresponding author. E-mail: misbahmirza88@yahoo.com

MM, 0000-0002-0272-1616

ABSTRACT

In the industrial sector, productive and effective treatment of toxic dye-based color pollutants is a key issue. Lanthanum and neodymium substituted cobalt–strontium (Co–Sr) spinel ferrite ($Co_{0.5}Sr_{0.5}RE_xFe_{2-x}O_4$, $x = 0.00$ and 0.06) catalysts were synthesized and used to degrade Congo red and rhodamine B dyes from an aqueous solution mixture in this study. For this specific purpose, RE^{3+} ions substituted Co–Sr spinel ferrite nanoparticles with photocatalytic degradation ability were prepared through sol–gel method. The degradation of CR and RhB in recently synthesized nanoferrites was also examined. SEM and XRD were used to characterize the prepared samples. The optical band gap values of synthesized spinel ferrites were examined with the help of Tauc plots by using UV-visible absorption. It was determined that the energy bandgap ranged from 2.91 to 2.52 eV. For $Co_{0.5}Sr_{0.5}Fe_2O_4$, $Co_{0.5}Sr_{0.5}La_{0.06}Fe_{1.94}O_4$, and $Co_{0.5}Sr_{0.5}Nd_{0.06}Fe_{1.94}O_4$ nanoferrites, the rates of CR and RhB dye degradation were 73–90% and 45–85%, respectively, at pH 5–7. The kinetics models successfully described the degradation reaction as pseudo-first-order kinetics. It was, therefore, concluded that the prepared samples can be used as effective photocatalysts in order to eliminate hazardous pollutants present in wastewater.

Key words: Congo Red, photocatalytic degradation, rhodamine B, spinel ferrite, UV–Vis spectroscopy

HIGHLIGHTS

- Rare-earth ion substitution spinel ferrite.
- Ferrite for degradation of dyes.
- Suitable band gap for photocatalytic purpose.

INTRODUCTION

Despite being a minor part of the electromagnetic spectrum ranging from 100 to 400 nm, ultraviolet radiation has a significant impact on living things (Diffey 2002). Furthermore, excessive ultraviolet light can have a major impact on plant photosynthesis (Hollósy 2002; Verdaguer *et al.* 2017). Recently, photocatalytic degradation of dangerous chemical compounds utilizing ultraviolet light and a semiconductor material has gotten a lot of interest. This strategy is a simple way to reduce river and ecosystem pollution (Schneider *et al.* 2014; Di Mauro *et al.* 2017). So, for the purpose of water purification, degradation through photocatalysis is the most efficient solution for the elimination of a wide variety of dyes in a wide range of concentrations; hence, this application is beneficial (Mironyuk *et al.* 2019a, 2019b).

Spinel ferrite is considered as an important study material because of its low band gap and photocatalytic activity in the visible light area for the removal of pollutants (Niu *et al.* 2015a). Cobalt–Strontium (Co–Sr) spinel ferrite is a unique magnetic substance that has been used in biological, electronic, and recording

technology (Bensebaa *et al.* 2004; Gao *et al.* 2009; Ahalya *et al.* 2014). Purity, shape, size, and attractive stability are all important factors in the photocatalytic activity and magnetic properties of ferrite nanoparticles (Haruna *et al.* 2020). Even though a large particle size of NPs may reduce photocatalytic activity by limiting the surface area of the catalyst, particles having smaller sizes likely to provide improved photocatalytic efficiency due to the high number of active sites (Giannakas *et al.* 2006). Ponraj *et al.* (2017) thoroughly discuss in their review article the work performed on the degradation of various dyes by using $BiFeO_3$ NPs. Further, they examined the surface phenomena of photocatalyst $BiFeO_3$, surface area (Wei *et al.* 2012; Soltani & Entezari 2013), and particle size (Gao *et al.* 2007; Liu *et al.* 2010; Gao *et al.* 2014; Niu *et al.* 2015b) and the way they impact photoactivity in their study on visible light-activated photocatalysts for the degradation of various textile dyes. The arrangement of divalent and trivalent ions in octahedral and tetrahedral locations determines the structure of spinel ferrite. Divalent compounds contain tetrahedral positions in normal spinel; however, in the inverse crystalline phase, the remaining trivalent ions occupy tetrahedral positions and the divalent ions occupy octahedral positions (Goldman 2006). Since several of the characteristics of ferromagnetic materials are reported to be influenced by the presence of impurity, significant research has been conducted that investigate the impact of cation contamination on the spinel ferrite lattice. The magnetic, electrical, and structural characteristics of ferromagnetic materials are altered when limited concentrations of these contaminants are added (Rana & Abbas 2002). Several studies have examined the effects of modifying the spinel crystalline structure of various ferromagnetic materials on their chemical characteristics as well as, as a result, magnetic permeability, their inherent characteristics of magnetization, anisotropy, electrical resistivity, Curie temperature, and magnetic resonance. Co–Sr spinel ferrite nanoparticles with lanthanum and neodymium substitutes have received a lot of attention throughout the area of nanomaterials because of their increased magnetic and electrical characteristics (Melagiriyappa & Jayanna 2009; Ishaque *et al.* 2010; Zhang & Wen 2010). Rare-earth ions (La^{3+}, Nd^{3+}) are potential replacements for enhancing the characteristics of spinel ferrites. The rare-earth element's 4f shell is insulated by $5s^2 5p^6$ and is nearly completely unaffected through the prospective domain of neighboring molecules. The magnetic and electrical transport characteristics of Co–Sr spinel ferrite nanoparticles could be improved via replacing rare-earth elements and existing 4f–3d interactions (Rezlescu *et al.* 2000). When these are compared to undoped spinel ferrites, structural properties such as magnetization, saturation, coercivity, and retentivity as well as anisotropy, vary significantly (Kumar & Kar 2012).

Chahar *et al.* (2021) used the citrate precursor approach to make $Co_xZn_{1-x}Fe_2O_4$ nanoferrites with varying concentrations, $x = 0.00$, 0.01, 0.02, 0.03, 0.04, and 0.05. It was reported that the degradation efficiency of methylene blue reached 77% for $x = 0.05$, compared to the minimum of 65% for $x = 0.00$, in 60 min during exposure to sunlight. Vosoughifar & Kimiay (2016) reported the synthesis of $CuFe_{2-x}Nd_xO_4$ photocatalyst through a sol–gel auto-combustion process and examined that methyl orange was degraded by 65% when exposed to UV light for 80 min. Naik *et al.* (2020) reported the fabrication of $CoFe_2O_4$ nanoparticles by sol gel route and also investigated that after 150 min of radiation, MB and EB had degraded 97 and 88%, respectively, due to low bandgap properties of prepared ferrites. Dhiman & Singhal (2019) synthesized $CoRE_{0.02}Fe_{1.98}O_4$ (RE = Eu, Gd, and Dy) spinel ferrites via a simple sol–gel auto-combustion method. For the composition $CoEu_{0.02}Fe_{1.98}O_4$, the maximum degradation of more than 90% was examined for both SO and RBY dyes, respectively, during 100 min of sunlight exposure. Abdo & El-Daly (2021) prepared $Co_{0.5}Cu_{0.5}Sm_xFe_{2-x}O_4$ ($x = 0.00$, 0.03, 0.06, 0.09, 0.12, and 0.15) nanoferrites by the citrate combustion approach. The nanoferrites demonstrated a degradation efficiency of 94.36% for RhB dye within 270 min at a concentration of $x = 0.15$, compared to $Co_{0.5}Cu_{0.5}Fe_2O_4$, which was 21.94%.

Co-precipitation (Maaz *et al.* 2009), hydrothermal method (Yan *et al.* 2015), and solid-state method (Deraz & Hessien 2009) are some of the methods used to make magnetic nanoparticles. The sol–gel approach, on the other hand, allows for good size control as well as a broad selection of reaction conditions for more modification (Zhang *et al.* 2015). The potential of sol–gel synthesis of oxide materials to produce nanoparticles exhibiting a stable pattern of crystalline solids, crystallite dimensions, and substantial surface area (Zhang *et al.* 2015) has piqued attention, in addition to its cheap cost and simple method.

The two dyes tested in this research, Congo red and rhodamine B, are azo dyes that are widespread in wastewater from industries and are very hazardous to human beings, causing skin irritation, nausea, blood clots, and asthma (Yu *et al.* 2009; Tavakoli-Azar *et al.* 2020). As a result, researchers have a significant task and aim to eliminate or reduce such toxins from the environment.

The goal of this study is to use the sol–gel process to synthesize pure, and rare-earth ions (La^{3+}, Nd^{3+}) substituted Co–Sr spinel ferrites with general formula $Co_{0.5}Sr_{0.5}Fe_2O_4$, $Co_{0.5}Sr_{0.5}La_{0.06}Fe_{1.94}O_4$ and

$Co_{0.5}Sr_{0.5}Nd_{0.06}Fe_{1.94}O_4$ and to investigate its potential to degrade dyes in industrial water. Further, this study described the synthesis, characterization, and degradation efficiency of Congo red (CR) and rhodamine B (RhB) dyes.

EXPERIMENTAL WORK

Materials and synthesis

In a typical sol–gel method, components such as chlorides, carbonates, and nitrates are employed; however, only nitrates are utilized in this work. To synthesize an undoped $Co_{0.5}Sr_{0.5}Fe_2O_4$ ($x = 0.00$) and two doped samples with a cubic-spinel structure, $Sr(NO_3)_2$ purchased from DAEJUNG, citric acid $C_6H_8O_7$, $Co(NO_3)_2{\cdot}6H_2O$ purchased from UNI-CHEM, $Fe(NO_3)_3{\cdot}9H_2O$, $La(NO_3)_3{\cdot}6H_2O$, and $N_3NdO_9{\cdot}6H_2O$ (99.9%) purchased from Merck-Germany and ammonia are utilized. Nitrates are dissolved in deionized water to prepare solutions of desired samples based on stoichiometric calculations. Lanthanum and neodymium are doped at a concentration of $x = 0.06$ to synthesize samples with the chemical compositions $Co_{0.5}Sr_{0.5}La_{0.06}Fe_{1.94}O_4$, and $Co_{0.5}Sr_{0.5}Nd_{0.06}Fe_{1.94}O_4$. To form a homogeneous mixture, the samples' solutions were prepared, and a magnetic stirrer was employed for constant stirring for about 10–20 min. After mixing well and preparing appropriate amounts of solution in three separate beakers, they were placed on magnetic hotplates. To keep the pH between 7 and 8, (35%) ammonia with a molarity of 51.67 mol/L was added randomly, drop by drop. The deionized water is evaporated from the solutions by heating below 80 °C and, once it evaporates, a dark brown wet gel is formed. It was then placed in an electrical thermostatic oven for 6 h approximately at 240 °C. To get loose powder, an agate mortar and pestle are employed. To achieve the final products, the fine powder is sintered in the furnace for 9 h at 950 °C. Schematic representation for the synthesis of $Co_{0.5}Sr_{0.5}RE_xFe_{2-x}O_4$ (x = 0.00 and 0.06) is shown in Figure 1".

Characterization techniques

The XRD patterns of prepared spinel ferrites were accumulated over the range from 20° to 70° of 2θ value by XRD analysis using a Bruker D Z Phaser (PW 1830) diffractometer. The microstructures are revealed using a VEGA3 TESCAN scanning electron microscope. The optical bandgap and degradation of CR and RhB dyes for pure and rare-earth (La, Nd) doped Co–Sr spinel ferrites were determined using UV visible spectroscopy (AE-S90-2D).

Photocatalytic activity

The photocatalytic degradation of CR and RhB was carried out when exposed to sunlight. To begin, 10 ppm CR and RhB dye solutions in 100 ml of deionized water were prepared in separate beakers and stirred for 10 min with a magnetic hot plate and continuous stirring. The solution mixtures were then combined with 20 mg of

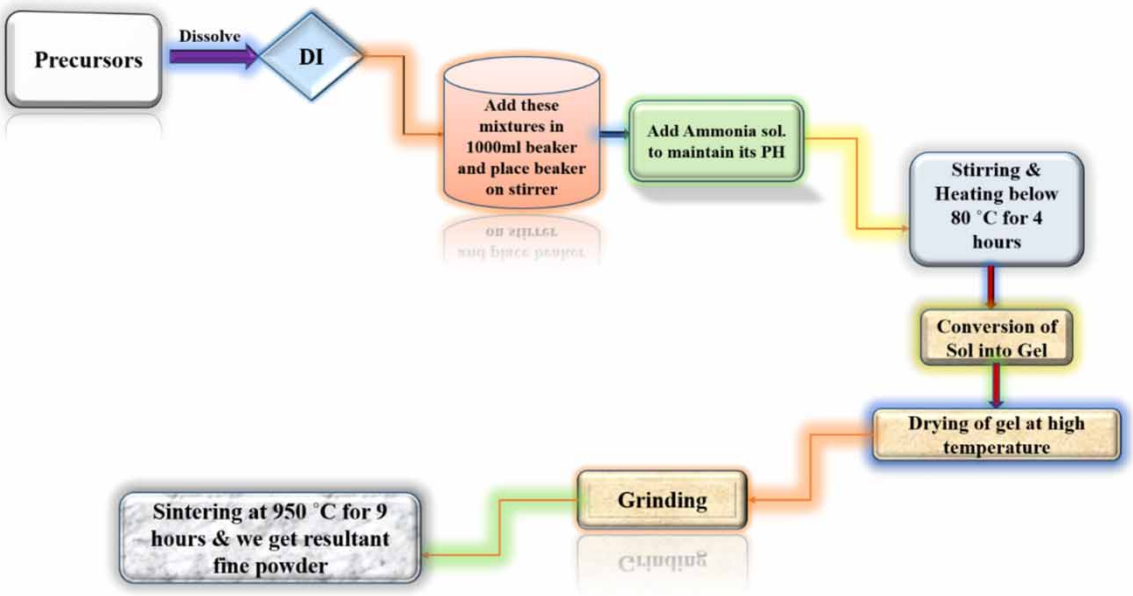

Figure 1 | Schematic representation for the synthesis of $Co_{0.5}Sr_{0.5}RE_xFe_{2-x}O_4$ ($x = 0.00$ and 0.06).

the photocatalyst. Before sunlight exposure, the solutions were kept in the dark on magnetic stirrers for about 30 min to examine the contribution of absorption. And then, after a dark reaction, from the solutions took a 4 ml sample in a falcon tube with no sunlight at a pH of about 5–7. After this, the dye solutions were exposed to sunlight for 60 min with continuous magnetic stirring and every 15 min, samples of dye solutions were taken in a tube. After this, by using UV-visible spectroscopy, the absorbance of CR and RhB after each time interval was examined. The degradation of CR and RhB is observed to follow pseudo-first-order kinetics, which is:

$$\ln\left(\frac{C_0}{C_t}\right) = kt \tag{1}$$

where the first-order rate kinetics is represented by k and initial concentration and concentration at any time t is represented by C_0 and C_t, respectively.

For each photocatalyst, the CR and RhB dye degradation percentages were calculated using the following equation:

$$(\%) = \left[\frac{(C_0 - C_t)}{C_0}\right] \times 100 \tag{2}$$

Here, C_0 → initial absorbance and C_t → final absorbance, respectively.

DISCUSSION OF THE FINDINGS

X-ray diffraction analysis

The X-ray diffraction patterns of $Co_{0.5}Sr_{0.5}RE_xFe_{2-x}O_4$, $x = 0.00$, and 0.06 are indicated in Figure 2(a)–2(c). For prepared spinel ferrites, the value of 2θ from these patterns is observed in the range of 20°–70° to determine its lattice constant, average crystallite size, cell volume, lattice strain, micro-strain, and dislocation density. The

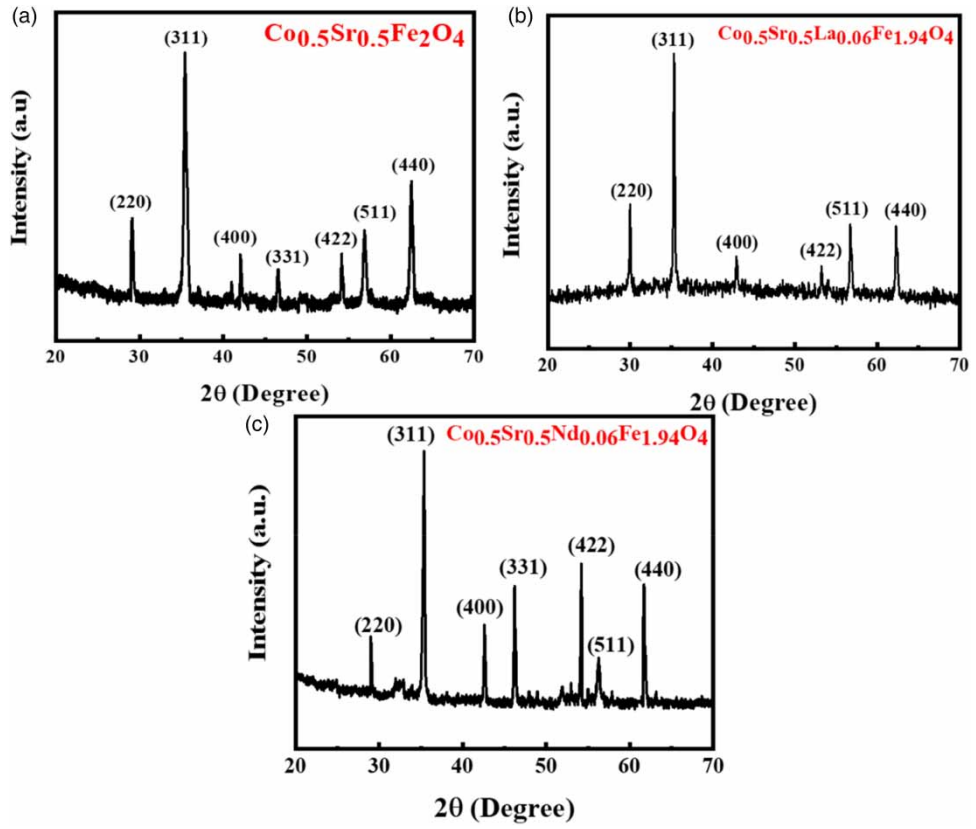

Figure 2 | X-ray diffraction patterns of $Co_{0.5}Sr_{0.5}Fe_2O_4$ (a), $Co_{0.5}Sr_{0.5}Nd_{0.06}Fe_{1.94}O_4$ (b), and $Co_{0.5}Sr_{0.5}La_{0.06}Fe_{1.94}O_4$(c) spinel ferrites.

patterns validated the presence of the prepared nanoparticles' cubic-spinel structure having a single phase and excluded out the possibility of any extra impurity peak. The reference card number 22-1086 was found to fit well with all of the diffraction peaks (220), (311), (400), (331), (422), (511), and (440). The classical Scherrer equation was applied to determine the average crystallite size (D) from the line width of the finest peaks:

$$D = \frac{k\,\lambda}{\beta\,\cos\theta} \tag{3}$$

Here, Scherer's constant is shown as $k = 0.9$, the wavelength is shown as λ, full-width half maximum (rad) is shown as β and Brag's angle is given as θ (Kokare *et al.* 2018).

The following formula can be utilized to derive the lattice parameter 'a' and volume 'V':

$$\alpha = d_{hkl}(h^2 + k^2 + l^2)^{1/2} \tag{4}$$

$$V = a^3 \tag{5}$$

where hkl denotes the miller indices values and 'd' denotes the gap between crystal planes.

The following formula is used to determine the lattice strain:

$$\varepsilon = \beta/4\tan\theta(10^{-3}) \tag{6}$$

In this case, θ denotes the peak's highest diffraction angle.

Micro-strain can be calculated using the following relationship:

$$\text{Micro}-\text{strain} = \beta\cos\theta/4(10^{-3}) \tag{7}$$

The following equation can be used to evaluate the dislocation density of the synthesized nanoparticles:

$$\delta = 1/D^2(10^{15}) \tag{8}$$

Here 'D' denotes for the crystalline size. Table 1 shows that the lattice parameter, cell volume, and average crystallite size all increase as lanthanum and neodymium ions are substituted. The findings for these structural properties are higher than those for pure Co–Sr spinel ferrite because of the formation of expansions and tensions inside the spinel structure. Additionally, the doping of La^{3+} and Nd^{3+} results in different values as a consequence of the higher ionic radii of lanthanum and neodymium ions over iron ions (Sharma *et al.* 2017). At the octahedral positions, La^{3+} and Nd^{3+} ions overlap with iron ions, which could have distorted the structure at the interstitial positions. As a result, the substitution of RE's metal ions may potentially affect structural properties like average crystallite size and lattice parameter. The values of lattice strain, micro-strain, and dislocation density decrease with the doping of lanthanum and neodymium, confirming that genuine spinel structure remains after the substitution of RE's metal ions (Yousaf *et al.* 2020).

Table 1 | Variation of structural parameters with La^{3+} and Nd^{3+} doping concentration of $Co_{0.5}Sr_{0.5}RE_xFe_{2-x}O_4$ ($x = 0.00$ and 0.06) ferrite samples

Parameters	$Co_{0.5}Sr_{0.5}Fe_2O_4$	$Co_{0.5}Sr_{0.5}\ La_{0.06}Fe_{1.94}O_4$	$Co_{0.5}Sr_{0.5}\ Nd_{0.06}Fe_{1.94}O_4$
Avg. crystalline size (nm)	31.51	36.59	36.60
Lattice parameter (Å)	8.37	8.41	8.39
Cell volume (a^3)	586.63	594.82	592.50
Dislocation density (lines/m) (10^{15})	1.0066	0.7467	0.7464
Lattice strain (10^{-3})	3.6036	3.1208	3.113
Micro-strain (lines^{-2}/m^{-4}) (10^{-3})	0.5441	0.3785	0.414

Morphological analysis

Figure 3 shows the SEM micrographs of undoped and rare-earth's doped Co–Sr ferrite nanoparticles. The microstructures of the as-synthesized samples were revealed through SEM data. Particles are micro-structured and irregularly shaped according to the surface morphology. The boundaries of most of the particles are not clear in the SEM pictures, and many particles are agglomerated. As a result, average particle diameters of 0.4, 0.63, and 0.75 μm were obtained for $Co_{0.5}Sr_{0.5}Fe_2O_4$, $Co_{0.5}Sr_{0.5}La_{0.06}Fe_{1.94}O_4$, and $Co_{0.5}Sr_{0.5}Nd_{0.06}Fe_{1.94}O_4$ by using image J processing software and Origin Pro software, whereas the histograms of particle distribution of prepared spinel ferrites are shown in Figure 3. It has been reported that the average particle diameter rises when RE's metal ions are substituted in spinel ferrite (Gharagozlou 2009). In addition, grain size distribution was observed to be inhomogeneous.

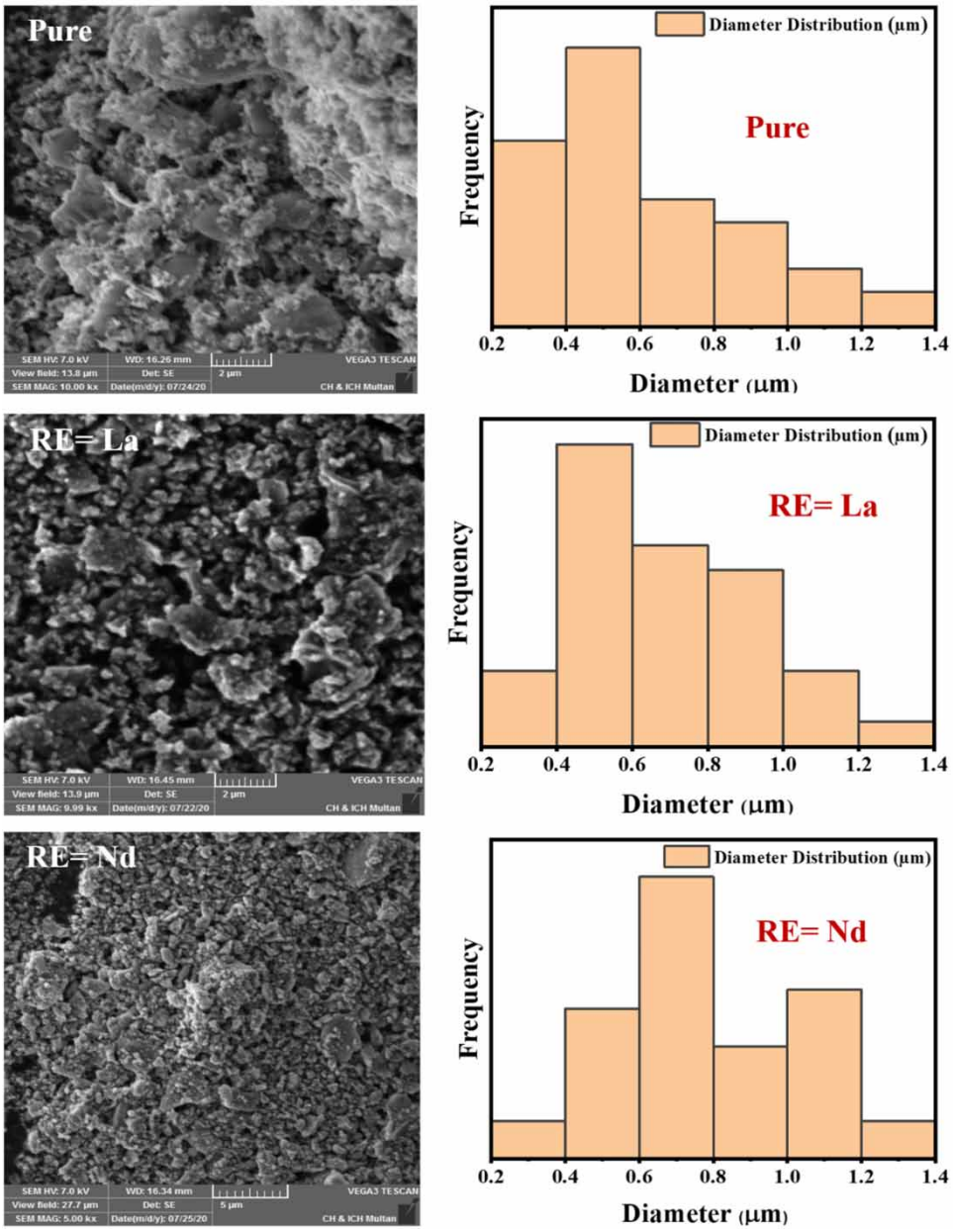

Figure 3 | SEM micrographs of pure and REs (La, Nd) doped Co–Sr spinel ferrite NPs, and SEM histograms for diameter distribution.

Optical analysis

The bandgap value of a semiconductor like spinel is important due to its optical and electrical properties in different applications, such as photocatalysis and photovoltaic devices. The optical characteristics, including bandgap, were shown to fluctuate with synthesis conditions and substitution (Das *et al.* 2010). Here, Tauc's relation is used to determine the optical bandgap:

$$\alpha h\nu = A(h\nu - E_g)^n \tag{9}$$

where α is the absorption co-efficient at a given wavelength λ, E_g shows the energy bandgap, h is the plank's constant, ν is the frequency of light, A is a constant, and n represents the possible direct transition with a value of 1/2. Graphs of $(\alpha h\nu)^2$ versus energy (eV) are shown in Figure 4, where the linear portion is extrapolated to the $h\nu$-axis to yield the energy bandgap (Nowsherwan *et al.* 2023). The bandgap values of the synthesized photocatalysts with and without La^{3+} and Nd^{3+} doping are also shown in Figure 4. The bandgap energy of pure $Co_{0.5}Sr_{0.5}Fe_2O_4$was determined to be 2.91 eV.$Co_{0.5}Sr_{0.5}La_{0.06}Fe_{1.94}O_4$ and $Co_{0.5}Sr_{0.5}Nd_{0.06}Fe_{1.94}O_4$ photocatalysts exhibited optical bandgaps around 2.62 and 2.52 eV, correspondingly. When compared to pure $Co_{0.5}Sr_{0.5}Fe_2O_4$, the bandgap energy of the La^{3+} and Nd^{3+} ions doped $Co_{0.5}Sr_{0.5}RE_xFe_{2-x}O_4$ nanoferrites was the lowest. Also, with the doping of La^{3+} and Nd^{3+} ions, the energy bandgaps reduced. And due to narrow bandgap value between 1.5 and 3 eV, ferrites are good for photocatalysis and have energy features that are beneficial for photocatalysis (López *et al.* 2015). So, these values of the energy bandgap make the photocatalysts highly efficient for dye degradation.

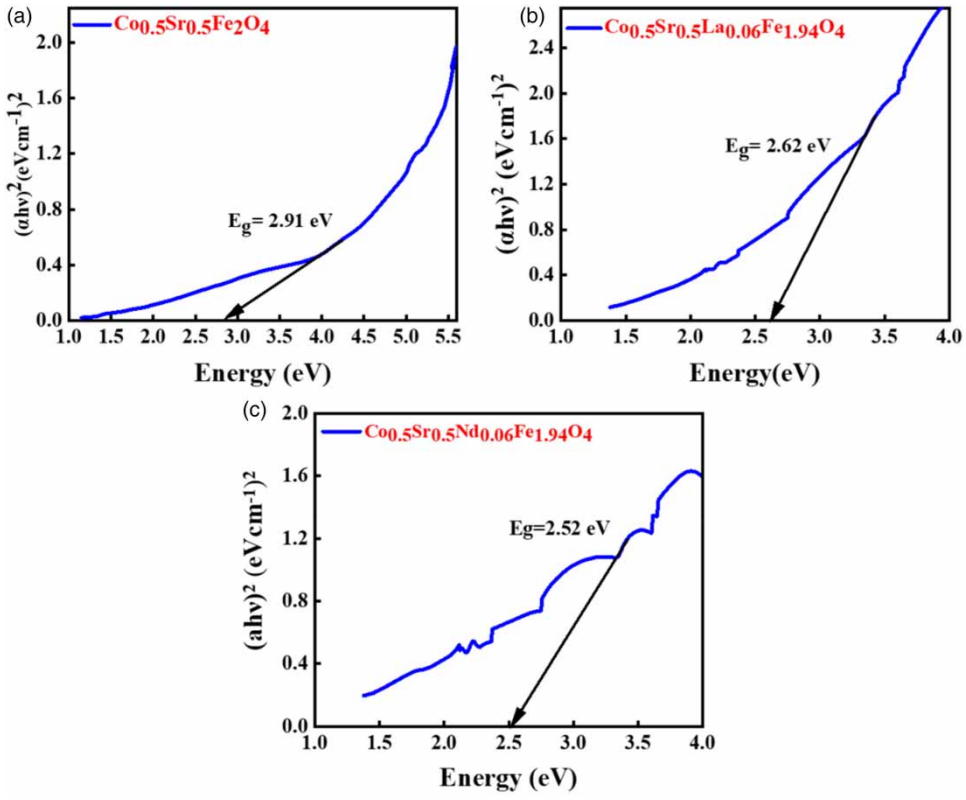

Figure 4 | (a–c) The Tauc's plot of $(\alpha h\nu)^2$ versus energy (eV) for undoped and rare-earth ions (La^{3+}, Nd^{3+}) doped Co–Sr spinel ferrites.

Photocatalytic study

Various studies have verified the role of spinel ferrite and its nanocomposites in the purification of contaminated water. Thus, these nanoferrites are simple to regenerate and may be reutilized several times before losing their quality, resulting in lower treatment costs. These spinel ferrites are also useful for photocatalytic activity due

to their narrow bandgap (<3 eV). When photons with higher energy are irradiated by sunlight, photo excitation occurs at the surface of the photocatalyst nanoparticles due to the equal number of holes and electrons created throughout the conduction and valence bands, resulting in the production of photogenerated electron–hole pairs. All this happens when the synthesized spinel ferrites have a bandgap energy value less than the energy of photons (Dong *et al.* 2015; Sun *et al.* 2019).

$$h\nu + Co_{0.5}Sr_{0.5}RE_xFe_{2-x}O_4 \rightarrow e^-_{CB} + h^+_{VB} \quad (\text{charge} - \text{pair generation}) \tag{10}$$

Depending on the oxidative environment and catalyst form, active free hydroxyl radicals are formed when H_2O species from the surrounding environment react with photogenerated holes in the valence band and thus serve as an oxidant by degrading organic pollutants directly (Dong *et al.* 2015; Lassoued *et al.* 2018; Sun *et al.* 2019). In the same way, anionic super-oxide specie is made by electrons in the conduction band through reduction when these electrons react with adsorptive oxygen on nanoparticle surfaces. After this, hydroperoxyl radicals are made by the combination of anionic super-oxide specie with H^+ or H_2O, which then dissociate into H_2O_2 and O_2 species (Li *et al.* 2011; Dong *et al.* 2015; Naik *et al.* 2019) Figure 5 represents the schematic illustration of photocatalytic degradation.

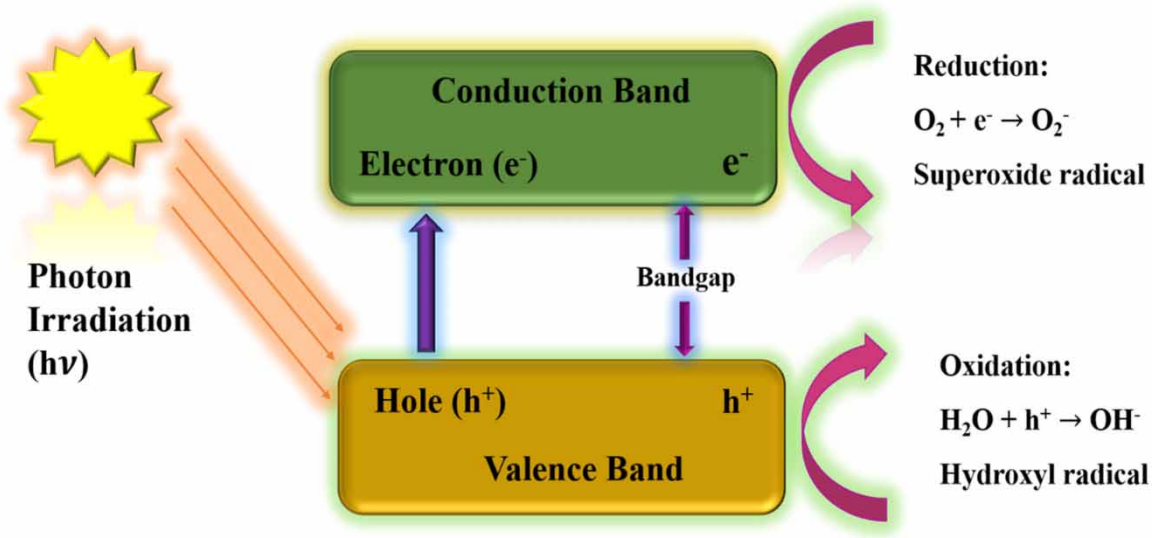

Figure 5 | Photocatalytic degradation is depicted during sunlight.

The degradation of RhB and CR was tested on the synthesized undoped and rare-earth ions (La, Nd) doped Co–Sr spinel ferrites. The typical UV–vis spectra of CR and RhB dyes during degradation of the prepared spinel ferrites are shown in Figures 6 and 7. The generation and separation of electron–hole pairs, absorption, and diffusion are the abilities on which the degradation of water traces depends (Kelly *et al.* 1999; Ahire *et al.* 2019). The percentage of degradation increased as the UV exposure time increased; the detailed description is stated in Table 2. Also, Table 2 lists the degradation percentage for CR and RhB solutions that use all of the ferrites. From the table, it is obvious that with the substitution of RE ions, the degradation of CR and RhB increases. The dye degradation was enhanced due to the narrow bandgap of rare-earth ions doped in Co–Sr spinel ferrite in comparison to the undoped spinel ferrite. According to the literature, the photocatalytic activity increases with decreasing energy bandgap (Huixian *et al.* 2011).

Figure 8(a) and 8(b) display the photocatalytic degradation of RhB and CR dyes, and degradation efficiency increases with time, reaching a maximum between 30 and 60 min for the rare-earth substituted Co–Sr spinel ferrites. As a result of this doping, defects and surface oxygen vacancies are formed, promoting photocatalytic degradation.

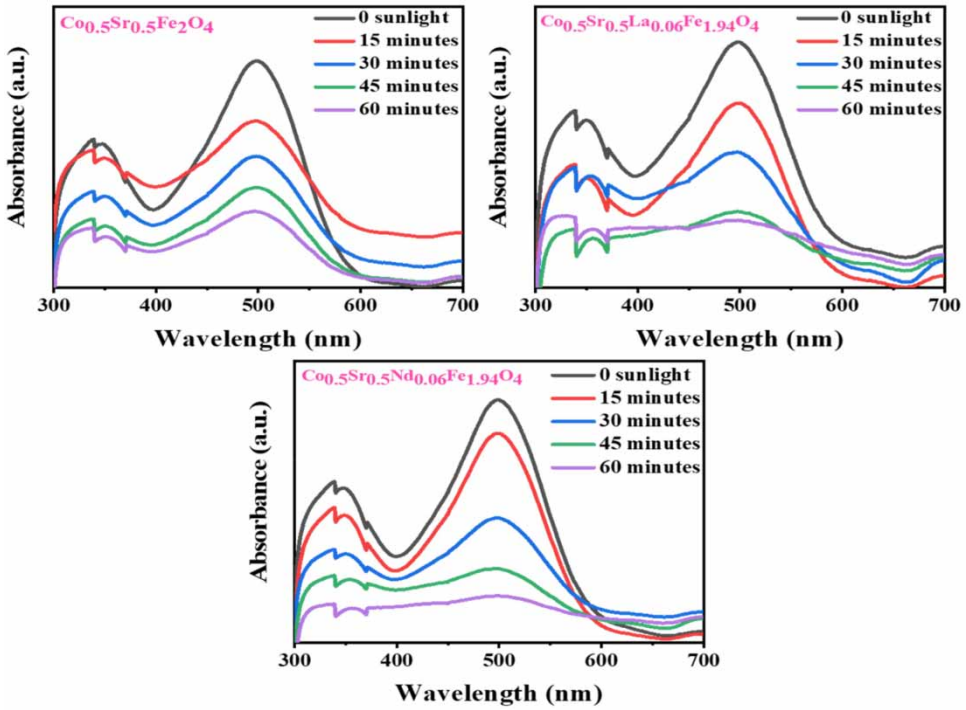

Figure 6 | Degradation profile of contaminant CR dye (UV–visible spectra) using $Co_{0.5}Sr_{0.5}Fe_2O_4$, $Co_{0.5}Sr_{0.5}La_{0.06}Fe_{1.94}O_4$, and $Co_{0.5}Sr_{0.5}Nd_{0.06}Fe_{1.94}O_4$ as photocatalysts.

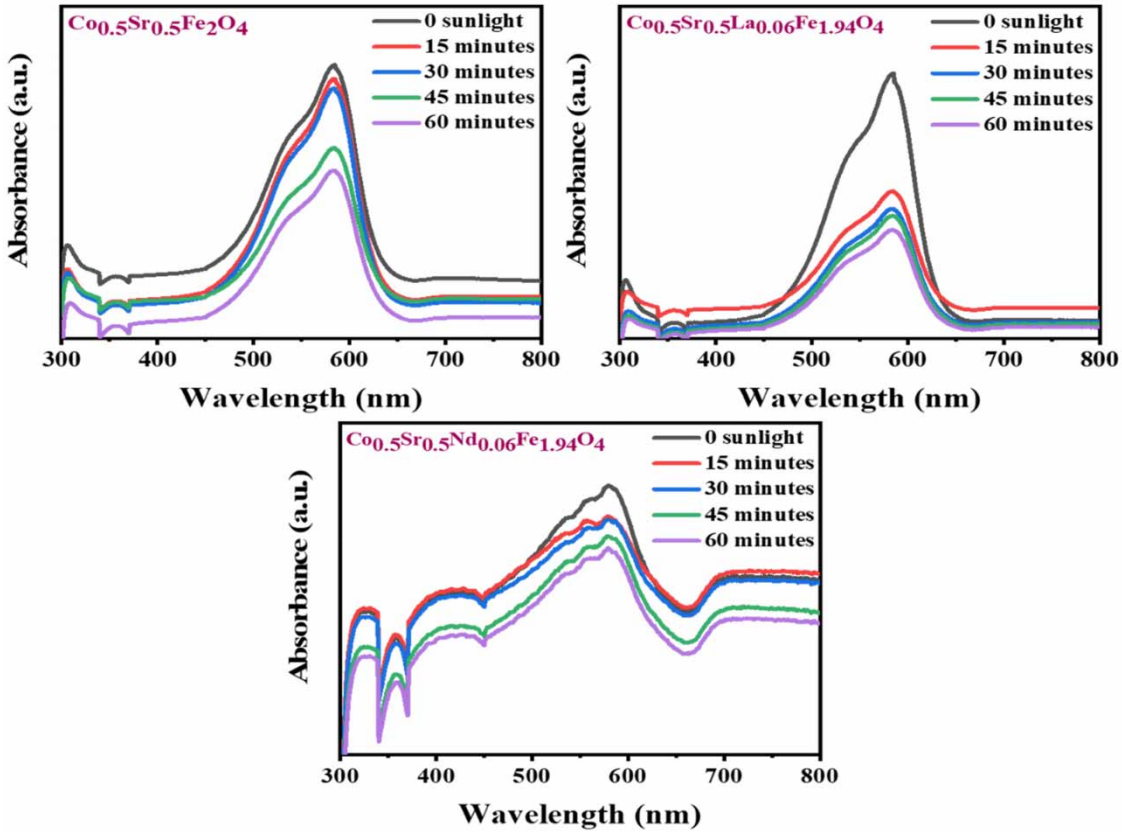

Figure 7 | The change in absorption of RhB solution with time in the presence of $Co_{0.5}Sr_{0.5}Fe_2O_4$, $Co_{0.5}Sr_{0.5}La_{0.06}Fe_{1.94}O_4$, and $Co_{0.5}Sr_{0.5}Nd_{0.06}Fe_{1.94}O_4$ photocatalysts under solar irradiation.

Table 2 | The degradation efficiency at various instants of time and pseudo-first-order rate constant for the photocatalytic degradation of cationic and anionic dyes

Ferrite composition	% Degradation RhB $t=15$	RhB $t=30$	RhB $t=45$	RhB $t=60$	CR $t=15$	CR $t=30$	CR $t=45$	CR $t=60$	Rate constant 'K' RhB	CR
$Co_{0.5}Sr_{0.5}Fe_2O_4$	5	9	35	45	29	45	60	73	0.002	0.007
$Co_{0.5}Sr_{0.5}La_{0.06}Fe_{1.94}O_4$	50	57	61	67	27	50	77	81	0.003	0.016
$Co_{0.5}Sr_{0.5}Nd_{0.06}Fe_{1.94}O_4$	40	46	67	85	15	53	76	90	0.016	0.025

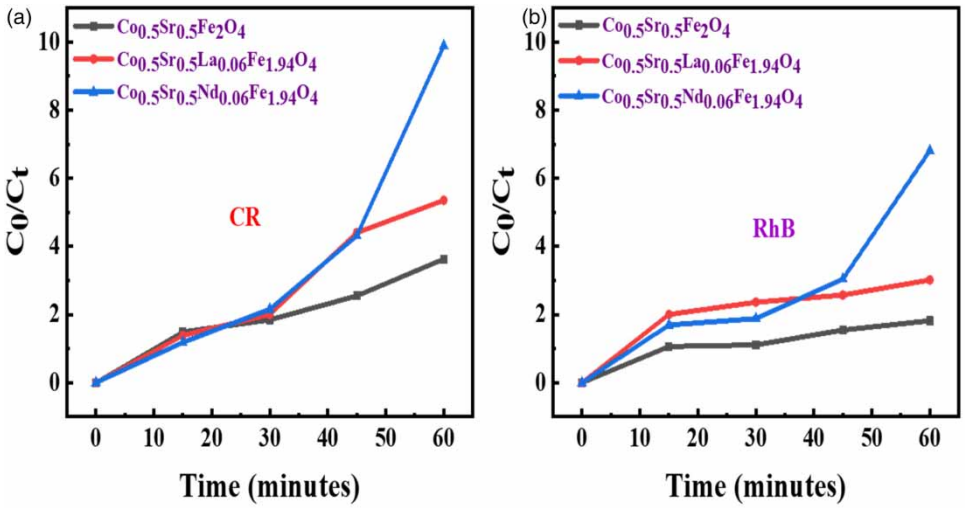

Figure 8 | C_0/C_t vs time for CR (a) and RhB (b) degradation utilizing $CO_{0.5}Sr_{0.5}RE_xFe_{2-x}O_4$ nanoferrites ($x = 0.00$, and 0.06).

The as-synthesized samples' $\ln(C_0/C_t)$ against time plot is shown in Figure 9(a) and 9(b). The photodegradation of CR and RhB is often observed to adopt pseudo-first-order kinetics. The highest values of rate constant were observed to be 0.016 and 0.025 min^{-1} for $Co_{0.5}Sr_{0.5}Nd_{0.06}Fe_{1.94}O_4$ for degrading RhB and CR according to

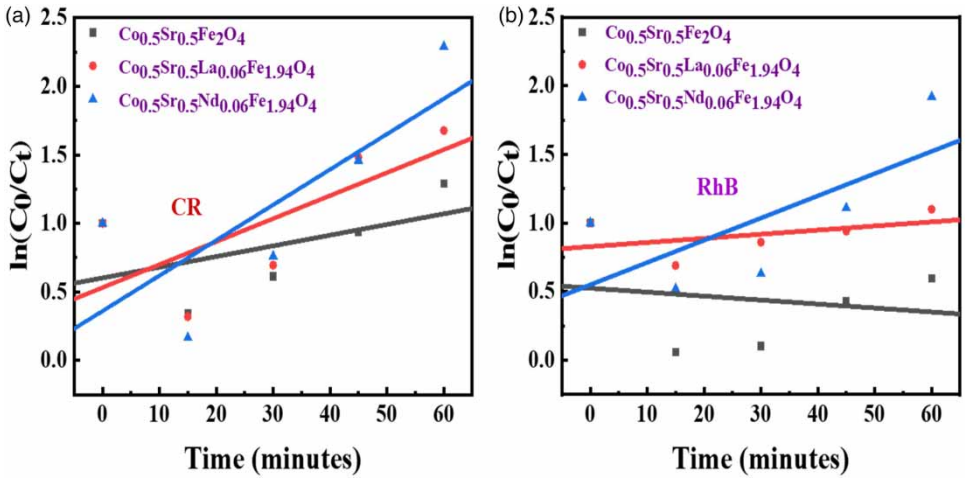

Figure 9 | (a,b) Pseudo-first-order kinetics of prepared photocatalysts.

Table 2. With increasing reaction time, the degradation rate also increased and the highest degradation occurred between 30 and 60 min. The photogenerated electrons released in the catalytic process exhibit significant deoxidizing and oxidizing characteristics due to lanthanum and neodymium doping in the Co–Sr ferrite lattice, and then maximum degradation of CR and RhB dyes is achieved. At the lattice's surface, as a result of a rise in defects and surface oxygen vacancies, this can happen. Another possibility is that metal ions are distributed differently at the octahedral and tetrahedral locations, affecting catalytic efficiency in the spinel ferrite as in A and B sites. As the catalytic activity is primarily dependent on metal ions in the B position, the catalytic efficiency for metal ions in the A position is often lower. At B sites, the reactant molecules interact more easily with metal ions because, at these sites, the metal ions are separated by a significant distance. When 'La^{3+}' and 'Nd^{3+}' ions are inserted separately into the Co–Sr ferrite lattice, these ions appear in the B positions, resulting in high catalytic efficiency due to the large concentration of lanthanum and neodymium ions (Ali *et al.* 2020).

Figure 10(a) and 10(b) show that the degradation of RhB and CR dyes increases over time for the prepared samples of 'La^{3+}'- and 'Nd^{3+}'-substituted Co–Sr spinel ferrites. The degradation efficiency improved over time, with significant degradation achieved in an hour for the obtained samples, as shown in Figure 10(a) and 10(b), respectively. Moreover, using the photocatalytic mechanism to degrade CR and RhB is a safe procedure. As the lanthanum and neodymium substituted Co–Sr spinel ferrites pose no environmental risk, water purification can be effectively done by using them.

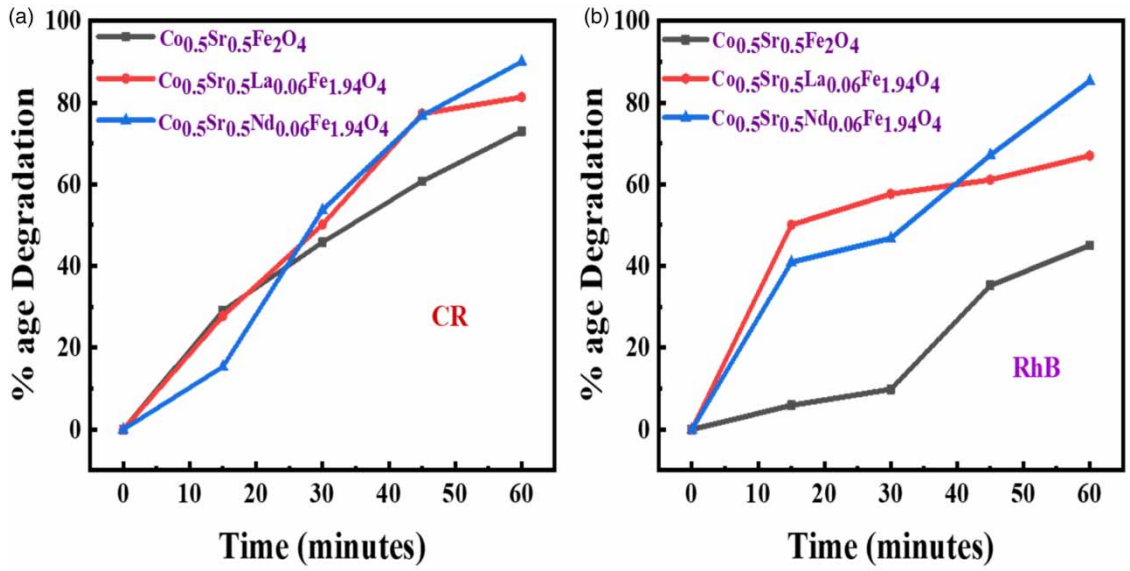

Figure 10 | Percent degradation efficiency of CR (a) and RhB (b) through $Co_{0.5}Sr_{0.5}RE_xFe_{2-x}O_4$ ($x = 0.00$, and 0.06) nanoparticles.

CONCLUSION

Pure and rare-earth metal ions (La, Nd)-substituted $Co_{0.5}Sr_{0.5}RE_xFe_{2-x}O_4$ ($x = 0.00$, and 0.06) nanoferrites were prepared using an inexpensive sol–gel approach. Powder XRD analysis demonstrates the emergence of single-phase face-centered cubic-spinel structures. Since REs have wider ionic radii than iron elements, the substitution of these cations alters the lattice parameter and crystalline size. By substituting REs^{3+}, the average crystallite size and optical energy bandgap values varied from 31 to 36 nm and from 2.91 to 2.52 eV, respectively. SEM analysis allowed for the identification of the microstructures of the synthesized ferrites. Inhomogeneous grains with average particle diameters ranging from 0.4 to 0.75 μm were seen in the SEM pictures of the prepared spinel ferrites. The substitution of La^{3+} and Nd^{3+} ions enhanced the degradation activity of the Co–Sr spinel ferrite samples. In this study, we achieved a significant improvement in the photocatalytic

Table 3 | Evaluation of photocatalytic degradation of present work with literature

Materials	Bandgap (Eg) (eV)	Dye	Time (min)	% Degradation	Reference
$Co_{0.7}Mg_{0.3}Ce_xFe_{2-x}O_4$ ($x = 0.00 - 0.1$)	1.53–1.57	MB	60	$x = 0.00$, 26.73%, $x = 0.04$, 74.94%, $x = 0.1$, 95.48%	Basfer & Al-Harbi (2023)
$La_xMnFe_{2-x}O_4$ ($x = 0.0,0.04$)	2.65–2.40	CV	150	$x = 0.00$, 32%, $x = 0.04$, 98%	Baig *et al.* (2020)
$NiCo_2O_4$(NCO), $Ni_{0.95}Ag_{0.05}Co_2O_4$(NACO), $Ni_{0.95}Ag_{0.05}Co_{1.95}La_{0.05}O_4$ (NACLO)	1.7–1.9	EB	150	NCO = 80%, NACO = 88%, NACLO = 98%	Priya *et al.* (2019)
$MSm_xFe_{2-x}O_4$,(M = Ni,Co; $x = 0$, 0.02, 0.06, 0.1)	<2	MO, SO	Ni (30 ~ 100), Co (30 ~ 100)	Ni (MO = 93–94%, SO = 92–95%), Co (MO = 91–95%, SO = 93–96%)	Singh *et al.* (2021)
$ZnAlFe_{1-x}Sm_xO_4$ ($x = 0$, 0.02, 0.04, 0.06, 0.08)	2.1–2.2	EB	240	$x = 0$, 20%, $x = 0.02$, 43%, $x = 0.04$, 60%, $x = 0.06$, 78%, $x = 0.08$, 58%,	Grecu *et al.* (2023)
$Co_{0.5}Sr_{0.5}RE_xFe_{2-x}O_4$ (RE = La, Nd; $x = 0$, 0.06)	2.91–2.52	RhB, CR	60	Pure (RhB = 45%, CR = 73%), La (RhB = 67%, CR = 81%), Nd (RhB = 85%, CR = 90%)	Present work

activity of CR and RhB dyes, attaining 90 and 85%, respectively. Amazingly, the nano-ferrite sample $Co_{0.5}Sr_{0.5-}Nd_{0.06}Fe_{1.94}O_4$ exhibited the highest percentages of CR and RhB degradation over the duration of 60 min because it had the lowest energy gap, and it can be used in treatments to clean up environmental pollutants effectively (Table 3).

ACKNOWLEDGEMENTS

This work is acknowledged by HEC-funded project NRPU#10408.

DATA AVAILABILITY STATEMENT

All relevant data are included in the paper or its Supplementary Information.

CONFLICT OF INTEREST

The authors declare there is no conflict.

REFERENCES

Abdo, M. & El-Daly, A. 2021 Sm-substituted copper-cobalt ferrite nanoparticles: preparation and assessment of structural, magnetic and photocatalytic properties for wastewater treatment applications. *Journal of Alloys and Compounds* **883**, 160796.

Ahalya, K., Suriyanarayanan, N. & Ranjithkumar, V. 2014 Effect of cobalt substitution on structural and magnetic properties and chromium adsorption of manganese ferrite nano particles. *Journal of Magnetism and Magnetic Materials* **372**, 208–213.

Ahire, S. A., Bachhav, A. A., Bagul, V. R., Ahire, B. B., Tupe, U. J. & Nashik, M. I. 2019 A literature review on: synthesis approaches of metal doped titanium dioxide **6**, 1238–1250.

Ali, N., Said, A., Ali, F., Raziq, F., Ali, Z., Bilal, M., Reinert, L., Begum, T. & Iqbal, H. M. 2020 Photocatalytic degradation of Congo red dye from aqueous environment using cobalt ferrite nanostructures: development, characterization, and photocatalytic performance. *Water, Air, & Soil Pollution* **231**, 1–16.

Baig, M. M., Zulfiqar, S., Yousuf, M. A., Touqeer, M., Ullah, S., Agboola, P., Warsi, M. F. & Shakir, I. 2020 Structural and photocatalytic properties of new rare earth La^{3+} substituted $MnFe_2O_4$ ferrite nanoparticles. *Ceramics International* **46**, 23208–23217.

Basfer, N. & Al-Harbi, N. 2023 Structural, optical and photocatalytic activity of Ce^{3+} doped Co–Mg nanoparticles for wastewater treatment applications. *Journal of King Saud University-Science* **35**, 102436.

Bensebaa, F., Zavaliche, F., L'ecuyer, P., Cochrane, R. & Veres, T. 2004 Microwave synthesis and characterization of Co–ferrite nanoparticles. *Journal of Colloid and Interface Science* **277**, 104–110.

Chahar, D., Taneja, S., Bisht, S., Kesarwani, S., Thakur, P., Thakur, A. & Sharma, P. 2021 Photocatalytic activity of cobalt substituted zinc ferrite for the degradation of methylene blue dye under visible light irradiation. *Journal of Alloys and Compounds* **851**, 156878.

Das, N., Ghosh, P., Mitra, M. & Chattopadhyay, K. 2010 Effect of film thickness on the energy band gap of nanocrystalline CdS thin films analyzed by spectroscopic ellipsometry. *Physica E: Low-Dimensional Systems and Nanostructures* **42**, 2097–2102.

Deraz, N. & Hessien, M. 2009 Structural and magnetic properties of pure and doped nanocrystalline cadmium ferrite. *Journal of Alloys and Compounds* **475**, 832–839.

Dhiman, M. & Singhal, S. 2019 Enhanced catalytic properties of rare-earth substituted cobalt ferrites fabricated by sol-gel auto-combustion route. *Materials Today: Proceedings* **14**, 435–444.

Diffey, B. L. 2002 Sources and measurement of ultraviolet radiation. *Methods* **28**, 4–13.

Di Mauro, A., Fragala, M. E., Privitera, V. & Impellizzeri, G. 2017 ZnO for application in photocatalysis: from thin films to nanostructures. *Materials Science in Semiconductor Processing* **69**, 44–51.

Dong, S., Feng, J., Fan, M., Pi, Y., Hu, L., Han, X., Liu, M., Sun, J. & Sun, J. 2015 Recent developments in heterogeneous photocatalytic water treatment using visible light-responsive photocatalysts: a review. *Rsc Advances* **5**, 14610–14630.

Gao, F., Chen, X., Yin, K., Dong, S., Ren, Z., Yuan, F., Yu, T., Zou, Z. & Liu, J. M. 2007 Visible-light photocatalytic properties of weak magnetic $BiFeO_3$ nanoparticles. *Advanced Materials* **19**, 2889–2892.

Gao, X., Liu, L., Birajdar, B., Ziese, M., Lee, W., Alexe, M. & Hesse, D. 2009 High-density periodically ordered magnetic cobalt ferrite nanodot arrays by template-assisted pulsed laser deposition. *Advanced Functional Materials* **19**, 3450–3455.

Gao, T., Chen, Z., Zhu, Y., Niu, F., Huang, Q., Qin, L., Sun, X. & Huang, Y. 2014 Synthesis of $BiFeO_3$ nanoparticles for the visible-light induced photocatalytic property. *Materials Research Bulletin* **59**, 6–12.

Gharagozlou, M. 2009 Synthesis, characterization and influence of calcination temperature on magnetic properties of nanocrystalline spinel Co-ferrite prepared by polymeric precursor method. *Journal of Alloys and Compounds* **486**, 660–665.

Giannakas, A., Leontiou, A., Ladavos, A. & Pomonis, P. 2006 Characterization and catalytic investigation of NO^+ CO reaction on perovskites of the general formula laxm1− xFeO3 (M = Sr and/or Ce) prepared via a reverse micelles microemulsion route. *Applied Catalysis A: General* **309**, 254–262.

Goldman, A. 2006 *Modern Ferrite Technology*. Springer Science & Business Media, New York, USA.

Grecu, I., Samoila, P., Pascariu, P., Cojocaru, C., Ignat, M., Dascalu, I.-A. & Harabagiu, V. 2023 Enhanced photodegradation of organic pollutants by novel samarium-doped zinc aluminium spinel ferrites. *Catalysts* **13**, 266.

Haruna, A., Abdulkadir, I. & Idris, S. 2020 Photocatalytic activity and doping effects of $BiFeO_3$ nanoparticles in model organic dyes. *Heliyon* **6**, e03237.

Hollósy, F. 2002 Effects of ultraviolet radiation on plant cells. *Micron* **33**, 179–197.

Huixian, S., Zhang, T. & Hongliang, W. 2011 Preparation and photocatalytic activity of La^{3+} and Eu^{3+} co-doped TiO_2 nanoparticles: photo-assisted degradation of methylene blue. *Journal of Rare Earths* **29**, 746–752.

Ishaque, M., Islam, M., Khan, M. A., Rahman, I., Genson, A. & Hampshire, S. 2010 Structural, electrical and dielectric properties of yttrium substituted nickel ferrites. *Physica B: Condensed Matter* **405**, 1532–1540.

Kelly, J., Kooij, E. S. & Meulenkamp, E. 1999 Luminescence studies of semiconductor electrodes. *Electrochimica Acta* **45**, 561–574.

Kokare, M., Jadhav, N. A., Kumar, Y., Jadhav, K. & Rathod, S. 2018 Effect of Nd^{3+} doping on structural and magnetic properties of Ni0.5Co0.5Fe2O4 nanocrystalline ferrites synthesized by sol-gel auto combustion method. *Journal of Alloys and Compounds* **748**, 1053–1061.

Kumar, L. & Kar, M. 2012 Effect of La^{3+} substitution on the structural and magnetocrystalline anisotropy of nanocrystalline cobalt ferrite ($CoFe_2$− xLa_xO_4). *Ceramics International* **38**, 4771–4782.

Lassoued, A., Lassoued, M. S., Dkhil, B., Ammar, S. & Gadri, A. 2018 Improved photocatalytic activities of CuxCo0.5-xNi0.5Fe_2O_4 nanoparticles through co-precipitation method in degrading methylene blue. *Physica E: Low-Dimensional Systems and Nanostructures* **101**, 29–37.

Li, X., Hou, Y., Zhao, Q. & Wang, L. 2011 A general, one-step and template-free synthesis of sphere-like zinc ferrite nanostructures with enhanced photocatalytic activity for dye degradation. *Journal of Colloid and Interface Science* **358**, 102–108.

Liu, Z., Qi, Y. & Lu, C. 2010 High efficient ultraviolet photocatalytic activity of $BiFeO_3$ nanoparticles synthesized by a chemical coprecipitation process. *Journal of Materials Science: Materials in Electronics* **21**, 380–384.

López, Y. O., Vázquez, H. M., Gutiérrez, J. S., Velderrain, V. G., Ortiz, A. L. & Martínez, V. C. 2015 Synthesis method effect of $CoFe_2O_4$ on its photocatalytic properties for H_2 production from water and visible light. *Journal of Nanomaterials* **16**, 76–76.

Maaz, K., Karim, S., Mumtaz, A., Hasanain, S., Liu, J. & Duan, J. 2009 Synthesis and magnetic characterization of nickel ferrite nanoparticles prepared by co-precipitation route. *Journal of Magnetism and Magnetic Materials* **321**, 1838–1842.

Melagiriyappa, E. & Jayanna, H. 2009 Structural and magnetic susceptibility studies of samarium substituted magnesium–zinc ferrites. *Journal of Alloys and Compounds* **482**, 147–150.

Mironyuk, I., Tatarchuk, T., Naushad, M., Vasylyeva, H. & Mykytyn, I. 2019a Highly efficient adsorption of strontium ions by carbonated mesoporous TiO_2. *Journal of Molecular Liquids* **285**, 742–753.

Mironyuk, I., Tatarchuk, T., Vasylyeva, H., Gun'ko, V. M. & Mykytyn, I. 2019b Effects of chemosorbed arsenate groups on the mesoporous titania morphology and enhanced adsorption properties towards Sr (II) cations. *Journal of Molecular Liquids* **282**, 587–597.

Naik, M. M., Naik, H. B., Nagaraju, G., Vinuth, M., Vinu, K. & Viswanath, R. 2019 Green synthesis of zinc doped cobalt ferrite nanoparticles: structural, optical, photocatalytic and antibacterial studies. *Nano-Structures & Nano-Objects* **19**, 100322.

Naik, M. M., Vinuth, M., Karthik, K., Suresha, B., Nagaraju, G. & Sujatha, H. 2020 Photocatalytic degradation of dyes by cobalt ferrite nanoparticles synthesized by sol-gel method. In *AIP Conference Proceedings*. AIP Publishing LLC, p. 040004.

Niu, F., Chen, D., Qin, L., Zhang, N., Wang, J., Chen, Z. & Huang, Y. 2015a Facile synthesis of highly efficient p–n heterojunction CuO/BiFeO3 composite photocatalysts with enhanced visible-light photocatalytic activity. *ChemCatChem* **7**, 3279–3289.

Niu, F., Gao, T., Zhang, N., Chen, Z., Huang, Q., Qin, L., Sun, X. & Huang, Y. 2015b Hydrothermal synthesis of bifeo3 nanoparticles for visible light photocatalytic applications. *Journal of Nanoscience and Nanotechnology* **15**, 9693–9698.

Nowsherwan, G. A., Zaib, A., Shah, A. A., Khan, M., Shakoor, A., Bukhari, S. N. S., Riaz, M., Hussain, S. S., Shar, M. A. & Alhazaa, A. 2023 Preparation and numerical optimization of TiO_2: CdS thin films in double perovskite solar cell. *Energies* **16**, 900.

Ponraj, C., Vinitha, G. & Daniel, J. 2017 A review on the visible light active bifeo3 nanostructures as suitable photocatalyst in the degradation of different textile dyes. *Environmental Nanotechnology, Monitoring & Management* **7**, 110–120.

Priya, A. S., Geetha, D., Karthik, K. & Rajamoorthy, M. 2019 Investigations on the enhanced photocatalytic activity of (Ag, La) substituted nickel cobaltite spinels. *Solid State Sciences* **98**, 105992.

Rana, M. U. & Abbas, T. 2002 The effect of Zn substitution on microstructure and magnetic properties of $Cu1- xZn_xFe_2O_4$ ferrite. *Journal of Magnetism and Magnetic Materials* **246**, 110–114.

Rezlescu, E., Sachelarie, L., Popa, P. & Rezlescu, N. 2000 Effect of substitution of divalent ions on the electrical and magnetic properties of Ni-Zn-Me ferrites. *IEEE Transactions on Magnetics* **36**, 3962–3967.

Schneider, J., Matsuoka, M., Takeuchi, M., Zhang, J., Horiuchi, Y., Anpo, M. & Bahnemann, D. W. 2014 Understanding TiO_2 photocatalysis: mechanisms and materials. *Chemical Reviews* **114**, 9919–9986.

Sharma, R., Thakur, P., Sharma, P. & Sharma, V. 2017 Ferrimagnetic Ni^{2+} doped Mg-Zn spinel ferrite nanoparticles for high density information storage. *Journal of Alloys and Compounds* **704**, 7–17.

Singh, S., Kaur, P., Kumar, V., Tikoo, K. & Singhal, S. 2021 Traversing the advantageous role of samarium doped spinel nanoferrites for photocatalytic removal of organic pollutants. *Journal of Rare Earths* **39**, 781–789.

Soltani, T. & Entezari, M. H. 2013 Sono-synthesis of bismuth ferrite nanoparticles with high photocatalytic activity in degradation of Rhodamine B under solar light irradiation. *Chemical Engineering Journal* **223**, 145–154.

Sun, M., Han, X. & Chen, S. 2019 Synthesis and photocatalytic activity of nano-cobalt ferrite catalyst for the photo-degradation various dyes under simulated sunlight irradiation. *Materials Science in Semiconductor Processing* **91**, 367–376.

Tavakoli-Azar, T., Mahjoub, A. R., Seyed Sadjadi, M., Farhadyar, N. & Hossaini Sadr, M. 2020 Synthesis and characterization of $CdTiO_3$@ S composite: investigation of photocatalytic activity for the degradation of crystal violet under sun light. *Journal of Inorganic and Organometallic Polymers and Materials* **30**, 667–683.

Verdaguer, D., Jansen, M. A., Llorens, L., Morales, L. O. & Neugart, S. 2017 UV-A radiation effects on higher plants: exploring the known unknown. *Plant Science* **255**, 72–81.

Vosoughifar, M. & Kimiay, A. 2016 Neodymium-doped copper ferrite: auto-combustion synthesis, characterization and photocatalytic properties. *Journal of Materials Science: Materials in Electronics* **27**, 10031–10035.

Wei, J., Zhang, C. & Xu, Z. 2012 Low-temperature hydrothermal synthesis of $BiFeO_3$ microcrystals and their visible-light photocatalytic activity. *Materials Research Bulletin* **47**, 3513–3517.

Yan, Z., Gao, J., Li, Y., Zhang, M. & Guo, M. 2015 Hydrothermal synthesis and structure evolution of metal-doped magnesium ferrite from saprolite laterite. *Rsc Advances* **5**, 92778–92787.

Yousaf, M., Akhtar, M. N., Wang, B. & Noor, A. 2020 Preparations, optical, structural, conductive and magnetic evaluations of RE's (Pr, Y, Gd, Ho, Yb) doped spinel nanoferrites. *Ceramics International* **46**, 4280–4288.

Yu, K., Yang, S., He, H., Sun, C., Gu, C. & Ju, Y. 2009 Visible light-driven photocatalytic degradation of rhodamine B over nabio3: pathways and mechanism. *The Journal of Physical Chemistry A* **113**, 10024–10032.

Zhang, Y. & Wen, D. 2010 Effect of RE/Ni (RE = Sm, Gd, Eu) addition on the infrared emission properties of Co–Zn ferrites with high emissivity. *Materials Science and Engineering: B* **172**, 331–335.

Zhang, Z., Yao, G., Zhang, X., Ma, J. & Lin, H. 2015 Synthesis and characterization of nickel ferrite nanoparticles via planetary ball milling assisted solid-state reaction. *Ceramics International* **41**, 4523–4530.

First received 30 November 2022; accepted in revised form 22 July 2023. Available online 2 August 2023